Addressed qubit manipulation in radio-frequency dressed lattices

2016 New J. Phys. 18 035009

(http://iopscience.iop.org/1367-2630/18/3/035009)

New Journal of Physics
The open access journal at the forefront of physics

Deutsche Physikalische Gesellschaft DPG
IOP Institute of Physics

Published in partnership with: Deutsche Physikalische Gesellschaft and the Institute of Physics

OPEN ACCESS

RECEIVED
21 October 2015

REVISED
19 January 2016

ACCEPTED FOR PUBLICATION
15 February 2016

PUBLISHED
10 March 2016

PAPER

Addressed qubit manipulation in radio-frequency dressed lattices

G A Sinuco-León[1] **and B M Garraway**

Department of Physics and Astronomy, University of Sussex, Falmer, Brighton, BN1 9QH, UK
[1] Author to whom any correspondence should be addressed.

E-mail: g.sinuco@sussex.ac.uk

Keywords: atom trapping and manipulation, atom-chips, RF dressed potentials, atomic qubit gates

Abstract

Precise control over qubits encoded as internal states of ultracold atoms in arrays of potential wells is a key element for atomtronics applications in quantum information, quantum simulation and atomic microscopy. Here we theoretically study atoms trapped in an array of radio-frequency dressed potential wells and propose a scheme for engineering fast and high-fidelity single-qubit gates with low error due to cross-talk. In this proposal, atom trapping and qubit manipulation relies exclusively on long-wave radiation making it suitable for atom-chip technology. We demonstrate that selective qubit addressing with resonant microwaves can be programmed by controlling static and radio-frequency currents in microfabricated conductors. These results should enable studies of neutral-atom quantum computing architectures, powered by low-frequency electromagnetic fields with the benefit of simple schemes for controlling individual qubits in large ensembles.

1. Introduction

Coherent control of the motion and internal degrees of freedom of ensembles of cold atoms is a requirement shared by many diverse applications of atomtronics. Such capabilities are developing in recent years along the lines of two complimentary approaches. Firstly, optical potentials have been employed for atomic confinement and transport, defining potential landscapes with features of a scale set by the radiation wavelength [1]. Secondly, near-field radiation from microscopic structures also creates detailed potential landscapes even when the wavelength (radio-frequency (RF) and microwaves (MW)) exceeds the dimensions of the structure [2]. In all cases, it is generically desirable to develop the capacity to control subsets of the atomic ensemble without disturbing nearby regions. This problem has been studied with atoms in optical lattices (OLs) [3], where the quality of addressing can be quantified in terms of gate errors [4]. In contrast, in this work we theoretically investigate an addressing scheme for atoms trapped in a RF lattice produced by currents in microfabricated conductors [5] and quantify the quality of the scheme with criteria previously used in the context of OLs.

A building block towards the experimental demonstration of a quantum processor is the realisation of high fidelity single-qubit state preparation, gates and read out. Currently, several platforms are in the race to demonstrate this capability with error levels sufficiently low to support error correction schemes for universal quantum computing. With this aim in mind, MW manipulation of single isolated atomic qubits has been demonstrated as a reliable method for qubit manipulation, thanks in part, to the high degree of control over MW sources and other technical advantages. A step further in developing scalable quantum processors is the control of individual qubits in extended arrays. Following the theoretical proposal by Das Sarma [6], cold atomic ensembles loaded in OLs have seen a rapid development towards this goal. In short, individual control of qubits in an OL follows from focusing light beams onto selected sites. The AC Stark shift induced by an appropriately tuned focused beam is used to tune the qubit frequency to an applied MW field [4, 6–10]. So far, such a scheme has demonstrated gate fidelity of $\sim$0.9983(14) and cross-talk errors at the level of 0.002(9) [4]. However, this method suffers from three intrinsic drawbacks: high sensitivity to misalignment of the addressing beam and the lattice site, cross-talk errors arising from beam overlap to nearest neighbour sites, and loss of fidelity due to spontaneous emission: all of these producing errors at the level of 10^{-4} [6]. In addition, the scaling up of this

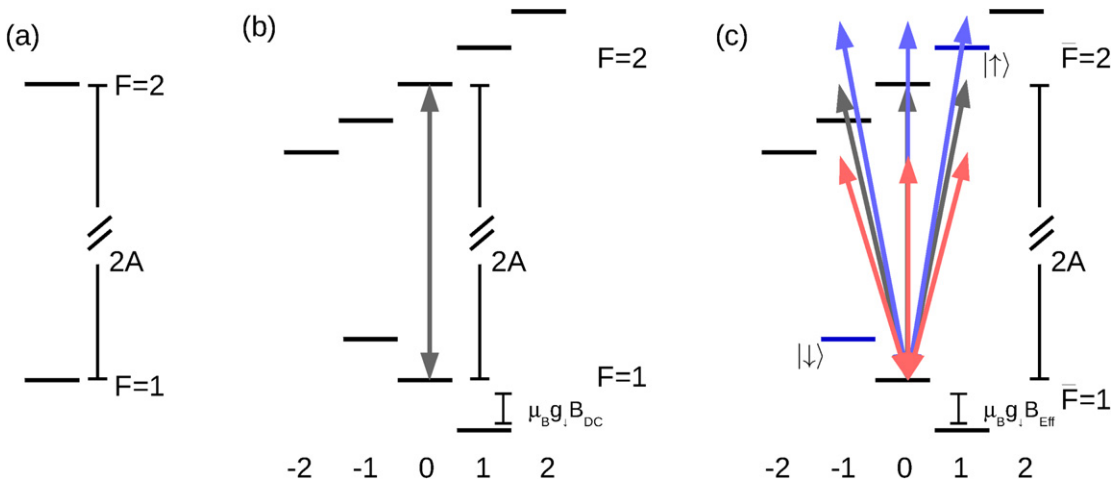

Figure 1. Ground state energy level structure of ^{87}Rb in different frames of reference. (a) Atomic frame of reference in absence of any field (free atom). (b) Atomic frame of reference with static and microwave magnetic field. The grey arrow indicates how a π polarised MW field couples two states with equal m_F but different total angular momentum, $\Delta F \neq 0$. (c) Atomic states in the dressed frame of reference (see text). Here, the original π polarised microwave field generates couplings among all dressed states (multiple grey arrows), as well as couplings at frequencies $\omega_{\rm MW} + m\omega_{\rm RF}$ (red and blue arrows) with integer m.

procedure to simultaneous independent control of a large number of sites presents a difficult engineering challenge.

Atom-chips are another favourable platform for controlling large ensembles of ultracold alkali atoms [2]. 1D and 2D periodic arrays of magnetic microtraps have been demonstrated experimentally, using thin layers of permanent magnetic materials to modulate the magnetic field in the vicinity of the chip and with atom–surface distances $\leqslant 10$ μm [11, 12]. Although in [12] single-site addressability has been achieved with a focused laser pulse, this route will share the difficulties mentioned for the case of OLs.

Adiabatic RF dressed potentials are an alternative platform for creating complex potential landscapes for ultracold alkali atoms and provide a mechanism for the accurate manipulation of atomic internal states [13]. Atom-chip configurations create fine tailored atomic potential landscapes by using static magnetic fields and low-frequency electromagnetic radiation, produced by permanent magnets and/or current carrying microfabricated conductors in close proximity to the atoms [14]. The excellent capabilities of these systems for coherent manipulation of quantum states stems from low sensitivity to noise and fabrication imperfections [15] as well as the achievable high degree of control over RF and DC current generators [16].

In this paper we theoretically study addressed control of atomic qubits in RF dressed lattices as proposed in [5]. After describing how MW radiation couples RF dressed states, we focus on qubits encoded by two dressed hyperfine states that experience similar dressed potentials. The qubit frequency, defined as the energy difference between the qubit states, can be locally controlled by currents in neighbouring conductors. In this way, rotations of the qubit at desired locations can be induced by resonant MW pulses. Here we also quantify the quality of this addressing scheme by randomised benchmarking [4, 17], and evaluate average gate fidelity and cross-talk errors due to implementation imperfections and near-surface magnetic noise.

2. ^{87}Rb interacting with static, RF and microwave magnetic fields

As a concrete example we present the case of ground state ^{87}Rb interacting with static, RF and MW magnetic fields. The corresponding ground state structure is shown in figure 1. ^{87}Rb has a nuclear angular momentum $I = 3/2$, which defines hyperfine manifolds with total angular momentum $F_\uparrow = I + 1/2 = 2$ and $F_\downarrow = I - 1/2 = 1$, separated by a hyperfine splitting of $\Delta E_{\rm hfs}/\hbar = 2\pi \times 6.8$ GHz. To describe the interaction with magnetic fields, it is convenient to group the atomic states in pairs of equal projection of total angular momentum, $m_F = m_I + 1/2$; that is states $\{|I, J, m_I, 1/2\rangle, |I, J, m_I + 1, -1/2\rangle\}$, where $|I, m_I\rangle$ denotes the nuclear angular momentum and $|J, \pm 1/2\rangle$ are states of electronic angular momentum.

The interaction with magnetic fields is parametrised by gyromagnetic factors. For the two hyperfine manifolds of ^{87}Rb, these factors correspond to linear Zeeman shifts of $\mu_B g_\uparrow/\hbar = 2\pi \times 702.37$ kHz G^{-1} and $\mu_B g_\downarrow/\hbar = -2\pi \times 699.58$ kHz G^{-1} [18]. Under conditions of a weak static magnetic field, the resonant coupling of states belonging to the same hyperfine manifold, i.e. $\Delta F = 0$, occurs at frequencies in the range of RF frequencies. In contrast, frequencies as high as MW are required for resonantly coupling Zeeman states of different total angular momentum, i.e. with $\Delta F = \pm 1$.

Having set the energy scales of interest, we consider the interaction of ^{87}Rb with a the time-dependent magnetic field of the form:

$$\boldsymbol{B}(t) = B_{\rm DC}\hat{\boldsymbol{z}} + \boldsymbol{B}_{\rm RF}\cos(\omega_{\rm RF}t + \phi_{\rm RF}) + \boldsymbol{B}_{\rm MW}\cos(\omega_{\rm MW}t + \phi_{\rm MW}), \tag{2.1}$$

where the direction of the z axis is defined by the static field, and the subscripts indicate the frequency of the different contributions: static (DC), RF and MW. The level population dynamics is determined by the Hamiltonian:

$$H = A\boldsymbol{I}\cdot\boldsymbol{J} + \mu_B\boldsymbol{B}(t)\cdot(g_I\boldsymbol{I} + g_J\boldsymbol{J}), \tag{2.2}$$

where $\boldsymbol{I}$ (g_I) and $\boldsymbol{J}$ (g_J) are the nuclear and electronic angular momentum operators (gyromagnetic factors), respectively. Taking the limit of weak static magnetic fields, the hyperfine gyromagnetic factors $g_{\uparrow,\downarrow}$ are expressed in terms of g_I and g_J [19]. The first term in (2.2) corresponds to the dipolar interaction between nuclear and electronic magnetic moments, and it is responsible for the hyperfine splitting $\Delta E_{\rm hfs}/\hbar = 2A/\hbar = 2\pi \times 6.8$ GHz in ^{87}Rb.

Initially we consider the interaction with static and RF fields and define the transformation from the basis $\{|I, J, m_I, m_J\rangle\}$ to the basis of RF dressed states, $\{|\bar{E}^{m_F}_{\uparrow,\downarrow}\rangle\}$. For this we proceed as follows. First, we determine the eigenstates of the atom interacting with the static magnetic field. For ground state alkali atoms this problem can be solved exactly, with eigenenergies given by the Breit–Rabi formula [19]:

$$E^{m_F}_{\pm} = -\frac{A}{4} + m_F\mu_B g_I B_{\rm DC} \pm \frac{1}{2}\sqrt{(A(I+1/2))^2 + 2m_F\mu_B B_{\rm DC}A(g_J - g_I) + (\mu_B B_{\rm DC}(g_J - g_I))^2} \tag{2.3}$$

and eigenstates corresponding to:

$$\begin{pmatrix}|E^{m_F}_{+}\rangle\\ |E^{m_F}_{-}\rangle\end{pmatrix} = \begin{pmatrix}\cos(\theta_{m_F}) & \sin(\theta_{m_F})\\ -\sin(\theta_{m_F}) & \cos(\theta_{m_F})\end{pmatrix}\begin{pmatrix}|I, J, m_I, 1/2\rangle\\ |I, J, m_I+1, -1/2\rangle\end{pmatrix} \tag{2.4}$$

with the rotation angle:

$$\tan(2\theta_{m_F}) = \frac{\sqrt{I(I+1) - m_F^2 + 1/4}}{(m_F + \mu_B B_{\rm DC}(g_J - g_I)/A)}. \tag{2.5}$$

The direct product of matrices (2.4) defines the transformation $U_{\rm Zeeman}$ between the basis of nuclear and electronic spins and the basis of Zeeman states, according to $\{|E^{m_F}_{\pm}\rangle\} = U_{\rm Zeeman}\{|I, J, m_I, m_J\rangle\}$.

Note that for weak static fields such that the energy difference between states of the same hyperfine manifold is small in comparison with the hyperfine splitting, i.e.:

$$E^{m_F}_i - E^{m'_F}_i \ll 2A, \quad \forall\, m_F, m'_F \quad \text{and} \quad i \in \{+, -\}, \tag{2.6}$$

the Zeeman states, $|E^{m_F}_{\pm}\rangle$, form two manifolds energetically well separated and in one-to-one correspondence to the hyperfine manifolds of the free atom $F_\uparrow = I + 1/2$ and $F_\downarrow = I - 1/2$. Therefore, under condition (2.6), the symbols $+$, $-$ in (2.3) can be identified with the projection of the electronic spin, and we use the symbols $\uparrow$, $\downarrow$ for the rest of the paper.

In the basis of Zeeman states defined by 2.4, the Hamiltonian, including only the interaction with the RF field, acquires the form:

$$H = \sum_{i\in\uparrow,\downarrow}\sum_{m_F} E^{m_F}_i\ |E^{m_F}_i\rangle\langle E^{m_F}_i| + \exp(i\omega_{\rm RF}t)\hat{V}_{\rm RF} + \exp(-i\omega_{\rm RF}t)\hat{V}^\dagger_{\rm RF}, \tag{2.7}$$

where $\hat{V}_{\rm RF} = U^\dagger_{\rm Zeeman}e^{i\phi_{\rm RF}}\boldsymbol{B}_{\rm RF}\cdot(g_I\boldsymbol{I} + g_J\boldsymbol{J})U_{\rm Zeeman}$.

To simplify the problem, we describe the atom–field interaction from the point of view of a frame of reference rotating around the z axis with frequency $\omega_{\rm RF}$. This is done by applying the unitary transformation:

$$U_{\rm R} = \exp(-i\omega_{\rm RF}t((g_\uparrow/|g_\uparrow|F^z_\uparrow + g_\downarrow/|g_\downarrow|F^z_\downarrow)) \tag{2.8}$$

with $F^z_{\uparrow,\downarrow}$ projection operators onto the two hyperfine manifolds:

$$F^z_\uparrow = \sum_{m_F=-(I+1/2)}^{I+1/2} m_F\ |E^{m_F}_\uparrow\rangle\langle E^{m_F}_\uparrow|, \tag{2.9}$$

$$F^z_\downarrow = \sum_{m_F=-(I-1/2)}^{I-1/2} m_F\ |E^{m_F}_\downarrow\rangle\langle E^{m_F}_\downarrow|. \tag{2.10}$$

The transformation of the interacting operators, $\exp(i\omega_{\rm RF})\hat{V}_{\rm RF} + \exp(-i\omega_{\rm RF})\hat{V}^\dagger_{\rm RF}$, is described in appendix A, (A.3). In short, in the rotating frame the interaction becomes the sum of one time-independent

component plus terms that oscillate at integer multiples of the frequency $\omega_{\rm RF}$ [20]. To obtain the final transformation to the basis of dressed states, we perform the rotating wave approximation (RWA), which neglects time-dependent terms in the rotating frame [20]. Thus, the Hamiltonian becomes:

$$H_{\rm RWA} = \sum_{i\in\uparrow,\downarrow}\sum_{m_F}\left(E_i^{m_F} - \frac{g_i}{|g_i|}\hbar\omega_{\rm RF}m_F\right)|E_i^{m_F}\rangle\langle E_i^{m_F}| + \hat{V}_{\rm RWA} + \hat{V}_{\rm RWA}^{\dagger}, \tag{2.11}$$

where $\hat{V}_{\rm RWA}$ is the static component of the operator $\exp(i\omega_{\rm RF}t)\hat{V}$ observed from the rotating frame. The dressed basis is defined as the eigenstates of Hamiltonian (2.11). Again, for off-resonant and weak inter-manifold coupling (that is for $\mu_B g_J|\boldsymbol{B}_{\rm RF}|$, $\mu_B g_{\uparrow,\downarrow}|\boldsymbol{B}_{\rm DC}| \ll 2A$), the dressed states form two manifolds well separated in energy, which correspond to the two possible projections of electronic spin. The basis transformation, $U_{\rm RWA}$, between Zeeman states, $\{|E_{\uparrow,\downarrow}^{m_F}\rangle\}$, and dressed states, $\{|\bar{E}_{\uparrow,\downarrow}^{m_F}\rangle\}$, is obtained as a solution of:

$$H_{\rm RWA}\ |\bar{E}_i^{m_F}\rangle = \bar{E}_i^{m_F}\ |\bar{E}_i^{m_F}\rangle. \tag{2.12}$$

For the present application, the dressed potential landscape corresponds to the energies $\bar{E}_i^{m_F}$ and it is obtained numerically by solving (2.12) at spatial locations with different field configurations. Following this procedure, our calculations include effects due to nonlinear Zeeman shifts and far off-resonant couplings between different hyperfine manifolds [21–23].

A slowly moving atom will adiabatically follow the dressed energy landscape defined by (2.12) if the following conditions is satisfied:

$$\hbar\omega_{x,y,z} \ll \min\mu_B|\boldsymbol{B}_{\rm RF}(\boldsymbol{r})| \ll \hbar\omega_{\rm RF}, \tag{2.13}$$

where $\omega_{x,y,z}$ represents the curvature of the dressed potential and the central term defines the minimal Larmor frequency in the rotating frame. The inequality on the left ensures adiabatic following of the energy surface defined by the dressed states, while the inequality on the right is required to apply the RWA, i.e. neglecting oscillating terms in the rotating frame [20].

2.1. Dressed energies in weak static fields

The standard definition of dressed states is established in the limit of linear Zeeman shifts [13, 20], where the Zeeman states are well approximated by eigenstates of the projection of total angular momentum F_z. Using this basis and the identity:

$$\mu_B\boldsymbol{B}_{\rm RF}\cdot(g_I\boldsymbol{I} + g_J\boldsymbol{J}) = \mu_B g_\uparrow\boldsymbol{B}_{\rm RF}\cdot\boldsymbol{F}_\uparrow + \mu_B g_\downarrow\boldsymbol{B}_{\rm RF}\cdot\boldsymbol{F}_\downarrow \tag{2.14}$$

with $\boldsymbol{F}_{\uparrow,\downarrow}$ the vector operator of total angular momentum, allows us to write the Hamiltonian as a linear combination of the components of the total angular momentum, F_x, F_y, F_z for each hyperfine manifold. A straightforward calculation shows that the static component of the Hamiltonian observed from a rotating frame is:

$$\hat{V}_{\rm RWA} = \frac{\mu_B g_\uparrow}{2}B_{{\rm RF},x}F_{\uparrow,x} + \frac{\mu_B g_\downarrow}{2}B_{{\rm RF},x}F_{\downarrow,x} \tag{2.15}$$

and the dressed states can be formed from the simple rotation:

$$U_{\rm RWA} = \exp(i\theta_\uparrow F_{\uparrow,y} + i\theta_\downarrow F_{\downarrow,y}) \tag{2.16}$$

with $\tan(\theta_i) = 1/2\mu_B g_i B_{{\rm RF},x}/(\mu_B g_i B_{\rm DC} - \hbar\omega_{\rm RF})$ for $i = \uparrow,\downarrow$.

Because of the linear approximation in the Zeeman shift, this last transformation can be performed analytically and defines the dressed energies in terms of an effective magnetic field:

$$\bar{E}_i^{m_F} = \mu_B g_i m_F B_{\rm Eff} = \mu_B g_i m_F\sqrt{\left(B_{\rm DC} - \frac{g_i}{|g_i|}\frac{\hbar\omega_{\rm RF}}{\mu_B}\right)^2 + \left(\frac{1}{2}B_{{\rm RF},x}\right)^2}$$

with $i = \uparrow,\downarrow$.

2.2. MW coupling of RF dressed states

To evaluate how MW magnetic fields couple RF dressed states, we start up with the full Hamiltonian in the Zeeman basis:

$$\begin{aligned} H = &\sum_{i\in\uparrow,\downarrow}\sum_{m_F}E_i^{m_F}\ |E_i^{m_F}\rangle\langle E_i^{m_F}| + \exp(\omega_{\rm RF}t)\hat{V}_{\rm RF} + \exp(-\omega_{\rm RF}t)\hat{V}_{\rm RF}^{\dagger} \\ &+ \exp(\omega_{\rm MW}t)\hat{V}_{\rm MW} + \exp(-\omega_{\rm MW}t)\hat{V}_{\rm MW}^{\dagger}. \end{aligned} \tag{2.17}$$

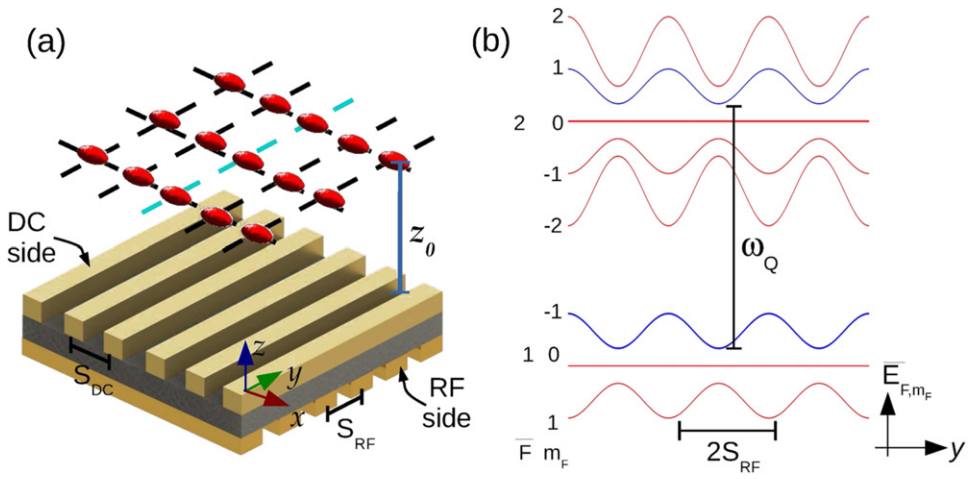

Figure 2. (a) Atom-chip layout and iso-energy surfaces corresponding to 1 μK. All conductors carry the same current amplitude producing a regular array of trapping wells for ^{87}Rb. (b) Dressed energies for ^{87}Rb along the line $x = 0$, $z = z_0$ (cyan dashed line in panel (a)). The horizontal axis represents position and the vertical axis indicates potential energy for the atoms. The dressed states $|\bar{E}^1_\uparrow\rangle$ and $|\bar{E}^{-1}_\downarrow\rangle$ experience approximately the same potential landscape (blue lines). The qubit frequency, ω_Q, is defined as the energy difference between the energy bottom of these two states.

In a frame of reference rotating at frequency ω_{RF} around the static field, the MW interaction becomes:

$$\hat{V}_{MW} \to U_R^\dagger \hat{V}_{MW} U_R = \hat{V}_{MW,R} = \sum_{\ell=-2(I+1/2)}^{2(I+1/2)} \exp(-\ell\omega_{RF} t + \omega_{MW} t)\hat{V}_\ell, \tag{2.18}$$

where the elements of $\hat{V}_{MW,R}$ can be calculated through (A.3).

Finally, by applying U_{RWA} calculated as a solution of (2.12), we obtain the MW interaction $\hat{V}_{MW,Dressed} = U^\dagger_{RWA}\hat{V}_{MW,R}U_{RWA}$ in the basis of the dressed states. This transformation does not modify the temporal dependence of equation (2.18), but establishes couplings between all the dressed states, as shown in figure 1(c). In the atomic frame of reference (panel 1(b)), a MW field π polarised with respect to the static field can only couple states satisfying $\Delta m_F = 0$. Since the dressed states are linear combinations of Zeeman states, the same MW field addresses all dressed states with additional components with frequencies of the form $\omega_{MW} + \ell\omega_{RF}$, with $\ell \in [-2(I+1/2),\ 2(I+1/2)]$.

3. Qubits encoded in a RF lattice

Here we consider an array of potential wells resulting from periodic modulation of the static and RF magnetic fields in equations (2.1) and (2.2). As shown in [5], such a modulation can be realised with a double layer atom-chip, in which arrays of conductors carrying DC/RF currents are fabricated on each face of the chip (see figure 2(a)). An additional uniform RF field removes regions with large non-adiabatic atomic losses and provides additional control over the geometry of the potential landscape [5]. Here we assume that control over the current of individual conductors of the chip is possible.

For concreteness, we consider the following setup: a double-layer atom-chip with each side containing 49 conductors of width 0.5 μm and height $h = 200$ nm, and where DC and RF conductors are separated by gaps of 3.5 μm and 1.5 μm, respectively (adding up to a centre-to-centre distance of $S_{DC} = 4.0$ μm and $S_{RF} = 2.0$ μm in figure 2). Each conductor carries a current density of $j_{DC,RF} \approx 3.71 \times 10^{10}$ A m^{-2}, producing a magnetic field of amplitude $B^0_{DC} = B^0_{RF} = 46.7$ G at its surface. The RF field is chosen to have angular frequency $\omega_{RF} = 2\pi \times 10.98$ MHz, which is resonant at a distance of $z_0 = 2$ μm from the surface of the central conductor on the DC side of the chip, from which all vertical distances are referred to. Finally, the set-up has a uniform external RF field with components $\boldsymbol{B}^E_{RF} = (17.51,\ 12.32,\ 0)$ G, which oscillates in phase with the RF currents. We numerically calculate the magnetic field distribution of this array, neglecting the thickness of both chip-substrate and conductors, but not the width of the conductor. For this calculation, we follow the procedure detailed in [5]. Note that this approximation is valid since we are interested in the field at distances one order of magnitude larger than the neglected parameters [24].

This design of currents and field produces a regular square array of potential wells (referred to as the RF lattice) with a period of 4 μm, trapping frequencies of $\frac{1}{2\pi}(\omega_x,\ \omega_y,\ \omega_z) = (38.2,\ 39.0,\ 78.9)$ kHz and minimal Larmor frequency of $\min \mu_B \left|\boldsymbol{B}_{RF}\right| = 2\pi\hbar \times 2.0$ MHz. Tunnelling between neighbouring wells is strongly

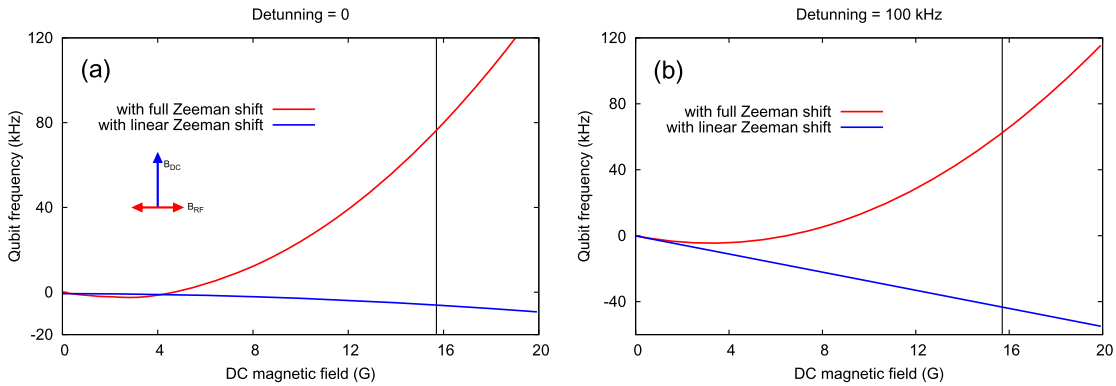

Figure 3. Qubit frequency as function of the static magnetic field, calculated using full (solid line) and linear (dashed) Zeeman shifts. (a) With resonant RF coupling $\omega_{\rm RF} = \mu_B g_\uparrow B_{\rm DC}/\hbar$; (b) with off-resonant RF coupling $\omega_{\rm RF} = \mu_B g_\uparrow B_{\rm DC}/\hbar + 2\pi \times 100$ kHz. In both panels $B_{{\rm RF},\perp} = 0.5$ G. The vertical line indicates the static field at which the regular array of wells is formed for the rest of the paper.

suppressed due to the large spacing and inter-well energy barrier $\sim 100\ \mu$K [6]. For the rest of the paper, we focus on sites at the centre of the array where fringe effects, associated with the finite number of conductors, are negligible [2]. The characteristics of this RF lattice are comparable with those of infra-red OLs, such as those recently realised in [4, 7].

Akin to magnetic traps, pairs of atomic states (one in each hyperfine manifold) experience approximately equal dressed potential landscapes. For ^{87}Rb, the RF lattice configuration can trap the hyperfine states $|\bar{E}^{-1}_{\downarrow}\rangle = |\downarrow\rangle$ and $|\bar{E}^{1}_{\uparrow}\rangle = |\uparrow\rangle$, at the bottom of the potential landscape sketched in figure 2(b) (blue lines). This allows us to encode qubit or clock states for applications in quantum information and MW clocks [11], in a similar way to magnetic and OLs. We define the qubit frequency $\omega_{\rm Q}$ as the energy difference between these two states at the bottom of the trapping well. In absence of any static and dressing fields, $\omega_{\rm Q}$ is equal to the hyperfine splitting ($2A$ in (2.2)). In the regime of linear Zeeman shifts (weak DC field, $B_{\rm DC} \approx 1$ G), the differential dressing of the qubit states is proportional to the difference between gyromagnetic factors of the two hyperfine manifolds, $g_\uparrow - g_\downarrow$, and corrections to $\omega_{\rm Q} = 2A/\hbar$ are negligible. However, for stronger DC fields ($B_{\rm DC} > 10$ G), nonlinear Zeeman shifts significantly affect the RF dressed potential due to the lifting of the degeneracy condition for resonant dressing [22, 23].

To quantify the effect of nonlinear Zeeman shifts over the qubit transition, we evaluate the deviation of $\omega_{\rm Q}$ from the hyperfine splitting using a simplified field configuration consisting of a static magnetic field $B_{\rm DC} \in [0,\ 20]\hat{\boldsymbol{z}}$ G and a dressing field $B_{\rm RF} = 0.5\hat{\boldsymbol{x}}$ G (see inset of figure 3(a)). We calculate $\omega_{\rm Q}$ from the eigenvalues of (2.12) and using the linear approximation (2.1), for resonant ($\omega_{\rm RF} = \mu_B g_\uparrow B_{\rm DC}/\hbar$) and off-resonant driving ($\omega_{\rm RF} - \mu_B g_\uparrow B_{\rm DC}/\hbar = -2\pi \times 100$ kHz). We observe that taking into account full Zeeman shifts, $\omega_{\rm Q}$ is significantly larger than the value obtained with linear Zeeman shifts. Also, the sensitivity of the qubit frequency to the static field (i.e. the gradient of the curves in figures 3(a) and (b)) is greatly enhanced in the case of nonlinear Zeeman shifts for $B_{\rm DC} > 10$ G: this effect being much pronounced in the case of resonant driving. For this particular set of parameters, which are within reach of atom-chip experimental setups, the qubit frequency scales with a curvature of $\frac{\partial^2 \omega_{\rm Q}}{\partial B^2_{\rm DC}} = 430$ Hz G^{-2} for resonant driving. Since our example of the RF lattice operates near resonance at a field of $B_{\rm DC} \approx 15.7$ G (vertical line in figure 3), these results indicate that $\omega_{\rm Q}$ can be effectively tuned by the currents applied to the conductors on the chip.

We test this idea by modifying the current of the central conductors at each face of the chip, in such a way that the conductor originally carrying DC (RF) current now has an additional RF (DC) component. More precisely the currents of conductors 1 and 2 in figure 4 are modified to produce static and RF fields of amplitude:

$$I_1 \rightarrow B^0_{{\rm DC},1} = 7.0\ {\rm G},\ B^0_{{\rm RF},1} = 43.4\ {\rm G}, \tag{3.19}$$

$$I_2 \rightarrow B^0_{{\rm DC},2} = 56.0\ {\rm G},\ B^0_{{\rm RF},2} = 3.0\ {\rm G} \tag{3.20}$$

at the surface of corresponding conductors. All other currents are kept as before.

With this new set of currents, the potential landscape is significantly modified above the selected conductors and in the neighbourhood of its crossing point. In general, the position of each dressed well is shifted from its original location and the trapping frequencies are modified. For illustration, numerical values of these parameters are shown in appendix B, table B1. Importantly, the additional currents make the qubit frequency different at each well, with differences of up to 20 kHz between neighbouring sites, corresponding to a gradient of $\frac{\partial \omega_{\rm Q}}{\partial x} \approx 5$ kHz μm^{-1}. This value is comparable to qubit (or clock) frequency variations obtained in infra-red

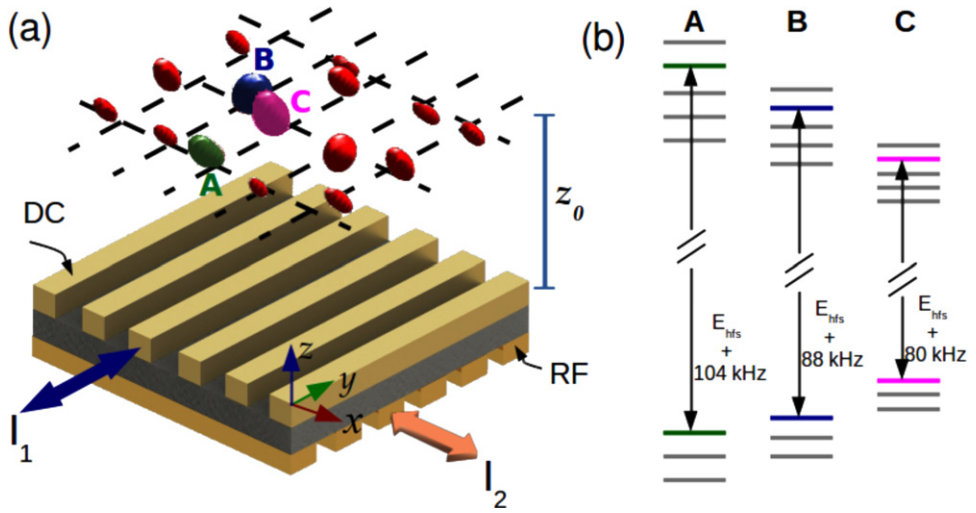

Figure 4. (a) Atom-chip layout and iso-energy surfaces corresponding to 1 μK. The current of two conductors is modified according to (3.20) (see text). (b) Dressed energy structure at sites **A** (blue) and **B** (green) in panel (a). Differences qubit frequency of these two sites occur due to the perturbation of the current distribution.

OLs where single site qubit manipulation have been demonstrated with highly focused laser radiation [4, 7]. In the RF lattice configuration, larger gradients of the qubit frequency can be obtained, in principle, by more drastic variations of the currents as well as employing larger current densities. However, this procedure is limited by ensuring that the dressed potential satisfies the conditions (2.13).

Note also that the RF lattice allows us to define complex patterns of qubit frequencies that can be engineered by specially tailored current patterns [25], allowing simultaneous control over the qubit state at various sites, using single or multiple MW frequencies. We can imagine, for example, that a current plus field configuration is set to produce equal qubit frequency at several sites and predefined fractions at others. In this situation, a monochromatic MW pulse will produce qubit rotations adjustable at each site. Furthermore, several MW frequencies can be used for addressing as well, as done in [3].

4. Addressed qubit manipulations with MW pulses

Control over the qubit frequency at different sites of the RF lattice allows us to induce addressed Rabi oscillations using MW pulses resonant at specific locations. We explore this possibility by solving numerically the interaction picture Schrödinger equation:

$$\mathrm{i}\hbar\,\partial_t\,|\psi(t)\rangle = \hat{V}_{\mathrm{MW,Dressed}}(t)|\psi(t)\rangle \tag{4.21}$$

at the trapping centre of sites of the modified RF lattice. The atomic state is expanded in the dressed basis:

$$|\psi(t)\rangle = \sum_{i\in[\uparrow,\downarrow]}\sum_{m_F} C_{i,m_F}(t)|\bar{E}_i^{m_F}\rangle, \tag{4.22}$$

with initial condition $|\psi(0)\rangle = |\uparrow\rangle$.

The population time-evolution is calculated at locations **A** (green), **B** (blue) and **C** (red) of figure 4. The MW is set to the lowest frequency resonant at location **A** in the dressed basis, i.e. at $\omega_{\mathrm{MW}} = \omega_{\mathrm{Q}}^{A} - 3\omega_{\mathrm{RF}}$, where the rotating frame is responsible for the displacement from the qubit frequency (see (A.3)). We study two MW polarisations: along the y and z axis, using a field of amplitude $|\boldsymbol{B}_{\mathrm{MW}}| = 3$ mG in both cases.

The population dynamics induced by this MW fields is shown in figure 5, where we plot the transition probability of the qubit $|\langle\downarrow|\psi(t)\rangle|^2$ calculated at sites **A**, **B** and **C**. We choose these sites because, with respect to **A**, they are the most (**B**) and least detuned (**C**), and the qubit frequency at all other sites falls within the range defined by this group. Large Rabi oscillations occur at **A**, while the probability of transferring population to the lower hyperfine state at non-resonant locations are smaller than 10^{-3}, and are barely noticeable at the scale of figures 5(a)–(b), but shown in panels (c) and (d). At all non-addressed sites, spurious excitation to dressed states out of the qubit basis are small because the MW field is detuned from resonance to those transitions, and require large MW amplitudes to become appreciable.

Qubit logic gates can be implemented with MW pulses. In figure 6 we plot the amplitude of probability in the qubit basis for the same MW field as in figure 5. We observe that MW pulses of duration $\approx$300 μs (vertical line in 6)

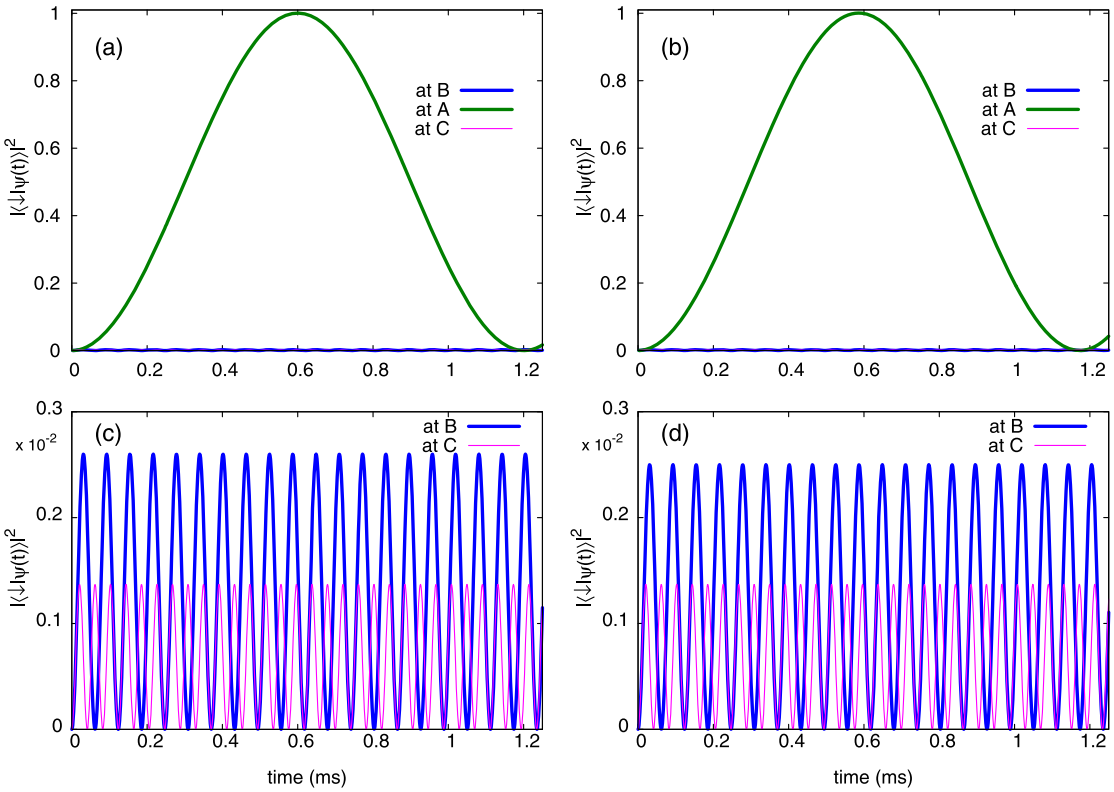

Figure 5. Rabi oscillations induced by a microwave field (a) and (c) linearly polarised parallel to the DC conductors and (b) and (d) linearly polarised MW transverse to the atom-chip. In all panels, the population probability are shown for sites **A** (green), **B** (blue) and **C** (pink), for a microwave field resonant at site **A**.

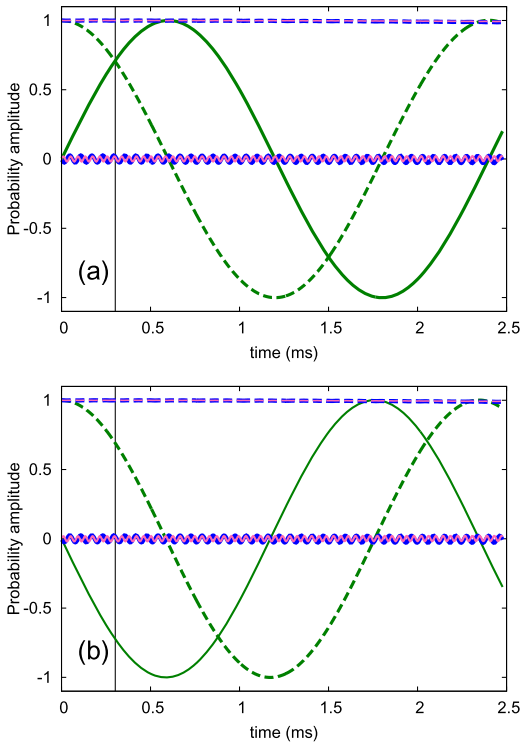

Figure 6. Time evolution of the amplitude of probability in the qubit basis, induced by a microwave field (a) real part of $\langle\downarrow|\psi(t)\rangle$ (solid) and $\langle\uparrow|\psi(t)\rangle$ (dashed) at sites A (green), B (blue) and C (pink) for a linearly polarised along the y direction (b) Imaginary part of $\langle\downarrow|\psi(t)\rangle$ (solid) and Real part of $\langle\uparrow|\psi(t)\rangle$ (dashed) as sites A (green), B (blue) and C (pink) for a microwave linearly polarised along the z direction. At site A, after 300 μs (vertical line) of interaction with a microwave field the qubit state performs rotations $R_y(\pi/2)$ and $R_x(\pi/2)$ in the Bloch sphere.

realise $\pi/2$ rotations of the Bloch vector around the x and y axis, depending on its polarisation. At non-resonant sites **B** and **C**, the MW field induces oscillations in the amplitude of probability with amplitude of the order 10^{-2}.

4.1. Average gate and cross-talk errors

Performing a large number of gates with small error thresholds is key for developing applications in quantum information with arrays of cold atoms. To identify the potential of the RF lattice as a computational architecture, we perform a benchmarking protocol over the set of Clifford operators $\mathcal{C}$ [4, 17], defined in appendix C. The 24 elements of the Clifford group are realised by composition of the Bloch rotations I, $R_x(\pm\pi/2)$, $R_y(\pm\pi/2)$, which can be implemented with MW pulses as describe above in figure 6. We use an implementation similar to [4], but in our case all pulses are defined with duration $\pi/2$ as shown in appendix C, table C1. With this, the average time of a Clifford gate is $\approx$675 μs.

We evaluate the average error per gate over the Clifford group resonantly tuned to site **A**, and calculate cross-talk error at sites **B** and **C** produced by off-resonant driving [26]. For our benchmark protocol, we create 32 random sequences of 128 elements selected uniformly from $\mathcal{C}$. For each sequence we set the initial state to $|\uparrow\rangle$ and apply truncated sequences of lengths $\ell \in [1, 16, 32, 48, 64, 80, 96, 112, 128]$. At the end of each truncated sequence we apply an additional operation corresponding to the inverse of the composition of the first ℓ gates, assuming error-free realisation. Since the Clifford set is a group, this last operation is also an element of the group. In our calculations, there is no dead time between Clifford gates. After each full sequence of length $\ell + 1$ we evaluate the fidelity, $\mathcal{F}$, defined as the projection of the final state onto the initial state $|\uparrow\rangle$:

$$\mathcal{F}(\ell) = |\langle\uparrow| \prod_{i=1}^{\ell+1} \mathcal{C}_i |\uparrow\rangle|^2 \tag{4.23}$$

with error-free sequences producing $\mathcal{F} = 1$. Results of this procedure for three different sites of the perturbed RF lattices are shown in figure 7.

The left column of figure 7 presents the full set of $\mathcal{F}$, calculated for each one of the 32 random sequences at sites **A**, **B** and **C** in figure 4. The average fidelity is shown on the right column and error bars corresponds to standard deviations.

The error probability per gate is evaluated at the addressed site, in this case site **A**, which is selected by tuning the MW in resonance to the qubit transition at this location. The average fidelity at **A** fits an exponential decay as the number of gates increases, providing information about the average error per gate. The fidelity fits the function [26]:

$$\mathcal{F}(\ell) = \frac{1}{2}(1 + (1 - d)^{\ell}) \tag{4.24}$$

with an error per gate of $\frac{d}{2} = 4 \times 10^{-4}$ [26]. Although the model of decay (4.24) assumes gate-independent and time-dependent errors [17], which is not the case since there are specific errors associated with the implementation of the qubit rotations, fitting of (4.24) describes the trend of the calculated decay suggesting an estimate of the error per gate in the dressed lattice. This level of error is also compatible with the error associated to energy shifts induced by coupling to states out of the qubit basis. Here, the qubit frequency shift is of <1 Hz and induces an error of 10^{-4} rad in the pulse area.

Ideal gates with zero cross-talk error leave the qubit state unperturbed at non-addressed sites. In the present case cross-talk errors has two origins: first, off-resonant MW coupling sets fast Rabi oscillations with small amplitude, which accounts for rotations of non-addressed qubits. Second, the MW field couples states out of the qubit basis (i.e. other dressed states) and after each pulse some population is transferred to these states. We fit the fidelity decay in figure 7 to the trial function:

$$\mathcal{F}(\ell) = 1 - \rho\ell - \Omega(1 - \cos(\theta_E \ell)). \tag{4.25}$$

The scattering of the data in figures 7(c) and (e) is due to coherent errors in the implementation of the gates [17]. The oscillation of (4.25) can be qualitatively understood as follows: each gate has a time-independent implementation error, which in the random sequence can be considered as a biased random walk of the angle between states resulting form applying ideal and MW realised element of the Clifford group. In this case the averages of the angle at **B** and **C** is $\theta_{\text{avg}} \approx 0.03$, which compares well to the fit values $\theta_{E,B} = 0.09$ and $\theta_{E,C} = 0.08$. We can guess $\theta_E > \theta_{\text{avg}}$ since the qubit polar angle performs a random walk biased by the non-uniform distribution of errors along the azimuthal direction [26].

The linear decay of the fidelity can be associated with a small population transfer to non-qubit states after each gate. The average reduction of the population in the qubit basis after applying one gate is $\rho_{\text{avg},B} = 0.001$ and $\rho_{\text{avg},C} = 0.002$, which compares well to the fitted values $\rho_B = 0.0009$ and $\rho_C = 0.001$. In this case $\rho_{\text{avg}} > \rho$ because the full reduction of the population in the qubit subspace occurs only during the first applied gate. Once implementation errors are optimally reduced (through pulse shape and duration as well as MW polarisation),

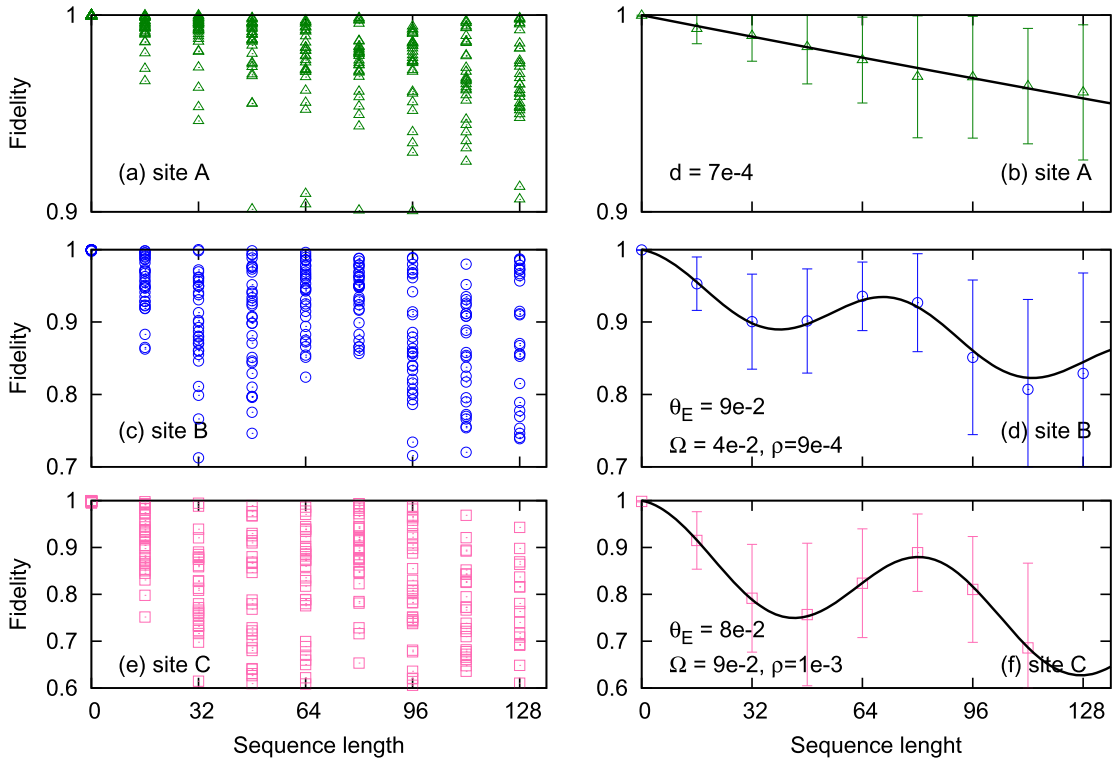

Figure 7. Fidelity of randomised sequences as function of the number of Clifford operations. Left column: full data set of 32 random realisations for each sequence length corresponding to sites (a) **A** (c) **B** and (e) **C**. Right column: average over 32 random realisations for sites (b) **A** (d) **B** and (f) **C**. Error bars are standard deviations from the full data set. Solid line corresponds to a fit to (b) equation (4.24) and (d) and (f) equation (4.25).

population transfer will remain as the main source of crosstalk error. Thus, a figure of merit for the crosstalk error per gate in the RF-lattice is at the level of $\rho = 10^{-3}$.

Imperfect implementation of qubit rotations leads to errors in gate operations, while cross-talk errors are due to off-resonant driving of non-addressed qubits. Both errors can be reduced by adjusting the MW polarisation and pulse duration [4, 26] and using quantum control techniques such as composite pulses [10]. A straightforward strategy for reducing the cross-talk error is to increase the qubit frequency difference between sites. This can be done by imposing more extreme modulations of the current distribution or setting the device in a region of stronger static field where the qubit frequency is more sensitive to the applied fields. Also, the current distribution can be optimised to obtain larger differences of the qubit frequency among neighbouring sites, similar to applications in ion qubit technology [25].

Our benchmarking protocol quantifies errors due to imperfect implementation of the Clifford group and population transfer out of the qubit basis. However, under experimental conditions there is a plethora of field sources that reduce gate fidelity. Technical noise in the phase and amplitude of MW and RF sources has been demonstrated to be small enough for coherent manipulation of quantum states in Bose–Einstein condensates [16], and this should be sufficient for the present case. Qubit manipulation can also be hindered by fluctuations of the environmental magnetic field that leads to fast fluctuations of the qubit frequency. This is particularly relevant for atom-chip technology due to the large amplitude of the magnetic field noise in the vicinity of conducting elements [14].

To estimate the impact of such an effect over the present application, we perform the benchmark protocol adding white Gaussian noise with a bandwidth of 1 GHz and variance of $\Delta B^2_{\rm rms} = 10^{-14}\ {\rm T}^2$. This level of noise is expected at 2 μm distance from a thin layer of Gold at 77 K [14, 27]. Results are shown in figure 8, where we note that the overall effect of the noise is to increase both the error per gate and the cross-talk error.

In order to define average error per gate in this situation, we fit the fidelity decay at site **A** to (4.24). Thus, average crosstalk error per gate at sites **B** and **C** are defined by fitting the fidelity decay to:

$$F_j = \frac{1}{2}(1 + e^{-2\rho_j \ell}) \tag{4.26}$$

with $\mathbf{j} = \mathbf{B, C}$, which is a model adequate for errors due to spurious excitations [26]. Resulting fits are shown as dashed lines in figure 8. Note that, in contrast to our previous fits shown in figure 7, in this case the fit is poor for sequences longer than 32 gates. However, an estimate of the error per gate can now be defined. At the addressed

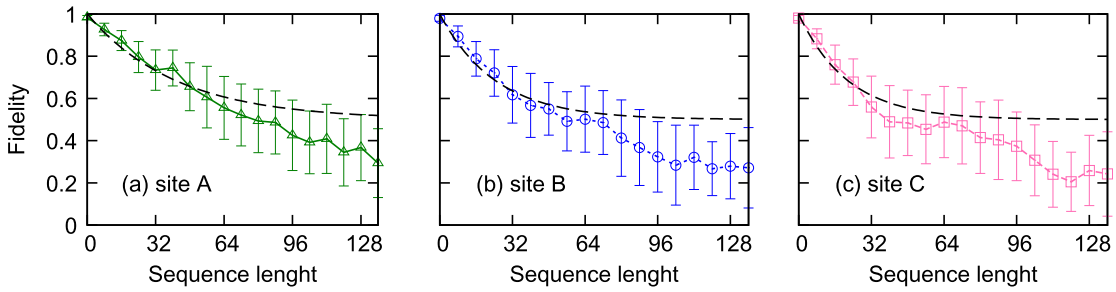

Figure 8. Fidelity of randomised sequences as function of the number of Clifford operations in presence of Gaussian white noise. Symbols corresponds to sites △ **A**, ∘ **B** and □ **C**. The data points corresponds to an average over 64 random sequences with different noise realisations. Lines are included to indicate the trend of the fidelity decay at each site. The noise is simulated as a normally distributed sequence of magnetic field, with variance $\Delta B^2_{\rm rms} = 10^{-14}$ T^2 and maximal frequency of 1 GHz, expected at 2 μm from a thin layer of Au at liquid Nitrogen temperature (77 K).

site, the error per gate in presence of noise becomes $\frac{d}{2} = 0.01$, and crosstalk error per gate at unaddressed sites is $\rho_B = \rho_C = 0.02$. The poor fitting of the fidelity decay to a single exponential function suggests that a more complex error model should be further investigated.

A more realistic evaluation of gate and cross-talk errors should consider channels for decoherence through a master equation. For RF dressed traps, non-adiabatic losses can be relevant in case of weak dressing field or fast modulation of trapping parameters. Understanding the sources of observed errors are key in devising strategies for improving the gate operation, but detailed error evaluation and sequence correction are beyond the scope of this work.

5. Outlook

The short atom–surface distance in atom-chips intentionally exposes the atoms to a large static magnetic field where nonlinear Zeeman shifts are relevant. The effect is sufficiently large as to allow us to tailor different potential landscape for states with similar (linear) magnetic susceptibility (i.e. the product $\mu_B g_F m_F$). In case of the RF lattice discussed in this work, nonlinear Zeeman shifts permit us to modulate the qubit frequency at different lattice sites by simply controlling the current of conductors in the atom-chip. Once we have control over the qubit frequency, addressed single-qubit manipulation can be implemented with resonant MW pulses. Our calculations indicate that the RF lattice have the potential for realising highly accurate quantum gates, with errors of the order of 10^{-4}, after controlling near-surface field noise. This approach allows simultaneous individual control of sites in a large array of qubits, simply by designing the pattern of currents in the atom-chip conductors. In addition, the intrinsic flexibility of RF dressed potentials can be exploited to create state dependent potentials and define two-qubit conditional phase gates, as suggested in [28]. For example, schemes for collisional gates can be implemented by modifying the current and field configurations in such a way that selected neighbouring lattice sites merge into a single one [5, 29]. Also, two-qubit gates between pairs of arbitrary lattice sites can be implemented with Rydberg gates, following the proposal for magnetic lattices in [11].

Further reduction of errors in gate implementation can be accomplished by borrowing techniques well known from nuclear magnetic resonance, which have been recently applied to control ensembles of ultracold atomic gases. For example, inhomogeneous control [10], optimised pulse duration and polarisation [4] and spin-echo [7], probed in OLs, can be straightforwardly applied to the present case. It is also desirable to reduce the average gate duration without increasing cross-talk errors. In general, this requires MW fields and qubit detuning larger than those considered here. Still, our calculation has been performed for a conservative set of parameters while the experimentally accessible range is substantially more ample, particularly in terms of the maximal current density supported by multilayer atom chips [30].

Near-surface noise is a major challenge for coherent manipulation with atom-chips [14]. However, developments in cryogenic atom-chip technology [31, 32] and materials science suggest that the next generation of atom-chips can see significantly reduced levels of noise. This can be achieved by using two-dimensional conducting materials such as 2D electron gases and graphene [33]. Similarly, thin patterned layers of permanent magnets can be employed as sources of static magnetic field, which, in principle, have reduced levels of noise associated with larger material resistivity [34]. A positive indication of this trend is the measurement of coherence times above 1 s at distances of $\sim$9 μm from a chip surface unprocessed to reduce field fluctuations [35]. Likewise, noise-sensitive gates can make an exceptional noise spectrum analyser capable for characterising and distinguishing various noise process [34, 36].

A potential drawback of the our scheme is the use of field sensitive states to encode the qubit, which make them sensitive to magnetic field noise. This effect can be reduced by defining gates which are sufficiently fast such that the accumulated phase induced by magnetic field fluctuations is small. Furthermore, high fidelity gates for qubits encoded in field-sensitive states has been demonstrated in OLs [7], suggesting that reducing magnetic field fluctuations in the atom-chip holds the key to unlock its potential as a computational architecture.

Acknowledgments

We gratefully acknowledge comments and input from Hiroki Takahashi, Thomas Fernholz, Mark Bason and Stefan Kuhr. This work was supported by EPSRC grant EP/I010394/1.

Appendix A. Zeeman states and AC magnetic fields: RWA

Consider an alkali atom interacting with a static magnetic field and one harmonically oscillating magnetic field, $\boldsymbol{B}_{\rm AC}\cos(\omega_{\rm AC}t+\phi_{\rm AC})$. In the basis of Zeeman states $|E_{\pm}^{m_F}\rangle$ defined by the static field, the Hamiltonian can be written as:

$$H=\sum_{i\in\uparrow,\downarrow}\sum_{m_F}E_i^{m_F}\ |E_i^{m_F}\rangle\langle E_i^{m_F}|+\exp(\mathrm{i}\omega_{\rm AC}t)\hat{V}+\exp(-\mathrm{i}\omega_{\rm AC}t)\hat{V}^{\dagger}, \tag{A.1}$$

where $\hat{V}=U_{\rm Zeeman}^{\dagger}\,\mathrm{e}^{\mathrm{i}\phi_{\rm AC}}\boldsymbol{B}_{\rm AC}\cdot(g_I\boldsymbol{I}+g_J\boldsymbol{J})\,U_{\rm Zeeman}$.

The dynamics of an atom interacting with an oscillating field can be simplified by performing a transformation to a frame of reference where the resulting Hamiltonian is dominated by a static component [37] . In the present case, a convenient selection of such a frame is one rotating around the direction of the magnetic field according to [21, 22]:

$$U_{\rm R}=\exp(-\mathrm{i}\Omega t((g_{\uparrow}/|g_{\uparrow}|F_{\uparrow}^{z}+g_{\downarrow}/|g_{\downarrow}|F_{\downarrow}^{z})) \tag{A.2}$$

where $F_{\uparrow,\downarrow}^{z}$ are defined in equation (2.10). The first term of Hamiltonian equation (A.1) is invariant under this transformation, while the elements of the interacting term, $\hat{V}_{\rm R}=U_{\rm R}^{\dagger}\mathrm{e}^{\mathrm{i}\omega_{\rm AC}}\hat{V}U_{\rm R}$ are given by:

$$\begin{aligned}
\langle E_{+}^{m_F'}|\ \hat{V}_{\rm R}(t)|E_{+}^{m_F}\rangle&=\exp(\mathrm{i}\Omega t(-m_F+m_F')+\mathrm{i}\omega_{\rm AC}t)\langle E_{+}^{m_F'}|\ \hat{V}\ |E_{+}^{m_F}\rangle\\
\langle E_{-}^{m_F'}|\ \hat{V}_{\rm R}(t)|E_{-}^{m_F}\rangle&=\exp(-\mathrm{i}\Omega t(-m_F+m_F')+\mathrm{i}\omega_{\rm AC}t)\langle E_{-}^{m_F'}|\ \hat{V}\ |E_{-}^{m_F}\rangle\\
\langle E_{+}^{m_F'}|\ \hat{V}_{\rm R}(t)|E_{-}^{m_F}\rangle&=\exp(\mathrm{i}\Omega t(m_F+m_F')+\mathrm{i}\omega_{\rm AC}t)\langle E_{+}^{m_F'}|\ \hat{V}\ |E_{-}^{m_F}\rangle\\
\langle E_{-}^{m_F'}|\ \hat{V}_{\rm R}(t)|E_{+}^{m_F}\rangle&=\exp(-\mathrm{i}\Omega t(m_F+m_F')+\mathrm{i}\omega_{\rm AC}t)\langle E_{-}^{m_F'}|\ \hat{V}\ |E_{+}^{m_F}\rangle,
\end{aligned}$$

where $\hat{V}_{\rm R}(t)$ denotes the interacting operator in the rotating frame. Similar transformation relations are obeyed by the operator $\mathrm{e}^{-\mathrm{i}\omega_{\rm AC}t}\hat{V}^{\dagger}$.

By setting the rotating frequency to $\Omega=\omega_{\rm AC}$, the elements in (A.3) that satisfy $|m_F\pm m_F'|=1$ become time-independent. These components dominate the dynamics when the coupling (divide by $\hbar$) is much smaller than the driving frequency $\omega_{\rm AC}$ [13, 20]. The RWA consists in keeping only those terms that are static in the rotating frame, resulting in the Hamiltonian:

$$H_{\rm RWA}=\sum_{i\in\uparrow,\downarrow}\sum_{m_F}(E_i^{m_F}-g_i/|g_i|\omega_{\rm AC}t)|E_i^{m_F}\rangle\langle E_i^{m_F}|+\hat{V}_{\rm RWA}+\hat{V}_{\rm RWA}^{\dagger}, \tag{A.3}$$

where $\hat{V}_{\rm RWA}$ is the the time-independent part of $\hat{V}_{\rm R}(t)$. The dressed states are defined as the eigenstates of $H_{\rm RWA}$ (A.3). The effect of cross manifold couplings is strongly suppressed by a large hyperfine splitting, such that the dressed states remain grouped in two hyperfine manifolds. The transformation from the atomic basis $|I,\ J,\ m_I,\ m_J\rangle$ to the dressed basis, $U_{\rm Dressed}$, is the composition of three transformation describe before, i.e $U_{\rm Dressed}=U_{\rm RWA}\,U_{\rm R}\,U_{\rm Zeeman}$, where $U_{\rm RWA}$ is the matrix of eigenvectors of $H_{\rm RWA}$.

When the rotating frequency $\Omega\neq\omega_{\rm AC}$, the interaction appears polychromatic, with a central angular frequency Ω and additional components displaced by integer multiples of ω up to $2F\times\omega$. The precise form of the matrix elements in the rotating frame is given by (A.3).

Appendix B. Parameters of the modified RF-lattice

In the uniform RF lattice, each site has the following properties:

$$\frac{1}{2\pi}(\omega_x, \omega_y, \omega_z) = (38.2,\ 39.1,\ 79.0)\ \text{kHz},$$
$$\text{Minimal Larmor frequency} = 2.0\ \text{MHz},$$
$$\frac{1}{2\pi}(\omega_{\text{Q}} - 2A/\hbar) = 82.9\ \text{kHz}$$

from which deviations occur in the perturbed lattice as shown in table B1 following the labeling in figure B1. Note that strong deviations with respect to the uniform values occur near the intersection of conductors where the current is modified. This allows us to calculate current and field distributions required to create predefined potential landscapes.

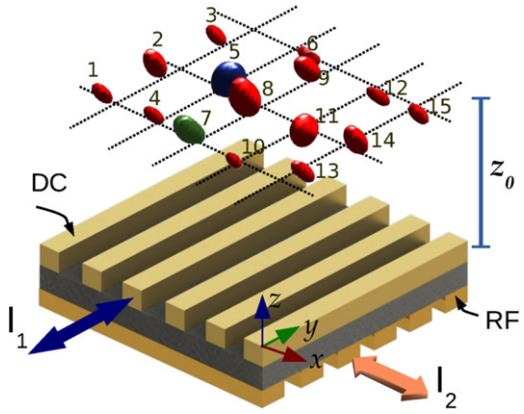

Figure B1. Labeling of displaced wells corresponding to table B1.

Table B1. Properties of the trapping wells in case of additional DC and RF current in a pair of crossed conductors. Sites labels are shown in figure B1.

Site	Displacement (μm)	$\frac{1}{2\pi}(\omega_x, \omega_y, \omega_z)$ (kHz)	Min. Larmor freq. (MHz)	$\frac{1}{2\pi}(\omega_{\text{Q}} - 2A/\hbar)$ (kHz)
1	(0.10, 0.03, −0.06)	(41.2, 42.1, 85.3)	2.1	83.4
2	(0.10, 0.03, 0.30)	(24.6, 27.8, 53.0)	3.2	86.9
3	(0.40, −0.06, −0.10)	(45.4, 46.8, 91.7)	1.9	82.9
4	(0.20, 0.06, −0.09)	(40.6, 37.5, 77.3)	2.8	86.8
5	(0.20, 0.06, 0.30)	(24.4, 26.4, 49.2)	3.6	88.5
6	(0.60, −0.06, −0.20)	(46.7, 44.2, 84.0)	2.4	85.4
7	(−0.10, 0.00, −0.10)	(22.1, 19.8, 45.1)	7.3	104.6
8	(0.00, 0.00, 0.40)	(16.7, 22.8, 33.3)	5.3	80.2
9	(0.10, 0.00, −0.10)	(22.1, 19.8, 45.1)	7.3	104.6
10	(−0.60, 0.06, −0.20)	(46.7, 44.2, 84.0)	2.4	85.4
11	(−0.20, −0.06, 0.30)	(24.4, 26.4, 49.2)	3.6	88.5
12	(−0.20, −0.06, −0.09)	(40.6, 37.5, 77.3)	2.8	86.8
13	(−0.40, 0.06, −0.10)	(45.5, 46.8, 91.7)	1.9	82.9
14	(−0.10, −0.03, 0.30)	(24.6, 27.8, 53.0)	3.2	86.9
15	(−0.10, −0.03, −0.06)	(41.2, 42.1, 85.3)	2.1	83.4

Appendix C. Elements of the Clifford group for qubits

Cross-talk errors and fidelity are evaluated using Randomized Benchmarking with over Clifford group shown in table C1. For a Rabi period of 1.2 ms, the average rotated angle $\langle\theta\rangle = \frac{27\pi}{24}$ corresponds to an average gate duration of $\tau_{\rm gate} = 675\ \mu$s.

Table C1. Elements of the Clifford group and its decomposition in single-qubit rotations: $\mathcal{C}_i = R_3 R_2 R_1$. Adapted from [4].

Index	U	R_3	R_2	R_1	θ	U^{-1} (index)
1	$\begin{pmatrix}1&0\\0&1\end{pmatrix}$	—	$R_x(-\pi/2)$	$R_x(\pi/2)$	π	1
2	$e^{-i\pi/4}\begin{pmatrix}1&0\\0&i\end{pmatrix}$	$R_x(\pi/2)$	$R_y(\pi/2)$	$R_x(-\pi/2)$	$3\pi/2$	16
3	$-i\begin{pmatrix}1&0\\0&-1\end{pmatrix}$	—	$R_x(\pi)$	$R_y(\pi)$	2π	3
4	$\begin{pmatrix}0&-1\\1&0\end{pmatrix}$	—	—	$R_y(\pi)$	π	4
5	$-e^{i\pi/4}\begin{pmatrix}0&1\\i&0\end{pmatrix}$	$R_x(\pi/2)$	$R_y(\pi/2)$	$R_x(\pi/2)$	$3\pi/2$	17
6	$-i\begin{pmatrix}0&1\\1&0\end{pmatrix}$	—	—	$R_x(\pi)$	π	6
7	$\frac{i}{\sqrt{2}}\begin{pmatrix}-1&-1\\-1&1\end{pmatrix}$	—	$R_x(\pi)$	$R_y(\pi/2)$	$3\pi/2$	18
8	$\frac{1}{\sqrt{2}}\begin{pmatrix}1&1\\-1&1\end{pmatrix}$	—	—	$R_y(-\pi/2)$	$\pi/2$	19
9	$\frac{e^{-i\pi/4}}{\sqrt{2}}\begin{pmatrix}1&1\\-i&i\end{pmatrix}$	—	$R_y(-\pi/2)$	$R_x(\pi/2)$	π	20
10	$\frac{-e^{i\pi/4}}{\sqrt{2}}\begin{pmatrix}1&1\\i&-i\end{pmatrix}$	—	$R_y(-\pi/2)$	$R_x(-\pi/2)$	π	21
11	$\frac{e^{-i\pi/4}}{\sqrt{2}}\begin{pmatrix}1&-1\\i&i\end{pmatrix}$	—	$R_y(\pi/2)$	$R_x(-\pi/2)$	π	22
12	$\frac{e^{i\pi/4}}{\sqrt{2}}\begin{pmatrix}1&-1\\-i&-i\end{pmatrix}$	—	$R_y(\pi/2)$	$R_x(\pi/2)$	π	23
13	$\frac{i}{\sqrt{2}}\begin{pmatrix}1&i\\-i&-1\end{pmatrix}$	—	$R_x(-\pi/2)$	$R_y(\pi)$	$3\pi/2$	13
14	$\frac{1}{\sqrt{2}}\begin{pmatrix}1&i\\i&1\end{pmatrix}$	—	—	$R_x(-\pi/2)$	$\pi/2$	24
15	$\frac{-i}{\sqrt{2}}\begin{pmatrix}1&-i\\i&-1\end{pmatrix}$	—	$R_x(\pi/2)$	$R_y(\pi)$	$3\pi/2$	15

References

[1] Ryu C and Boshier M G 2015 Integrated coherent matter wave circuits *New J. Phys.* **17** 092002
[2] Fortágh J and Zimmermann C 2007 Magnetic microtraps for ultracold atoms *Rev. Mod. Phys.* **79** 235
[3] Schrader D, Dotsenko I, Khudaverdyan M, Miroshnychenko Y, Rauschenbeutel A and Meschede D 2004 Neutral atom quantum register *Phys. Rev. Lett.* **93** 150501
[4] Xia T, Lichtman M, Maller K, Carr A W, Piotrowicz M J, Isenhower L and Saffman M 2015 Randomized benchmarking of single-qubit gates in a 2d array of neutral-atom qubits *Phys. Rev. Lett.* **114** 100503
[5] Sinuco-León G A and Garraway B M 2015 Radio-frequency dressed lattices for ultracold alkali atoms *New J. Phys.* **17** 053037
[6] Zhang C, Rolston S L and Sarma S D 2006 Manipulation of single neutral atoms in optical lattices *Phys. Rev.* A **74** 042316
[7] Wang Y, Zhang X, Corcovilos T A, Kumar A and Weiss D S 2015 Coherent addressing of individual neutral atoms in a 3d optical lattice *Phys. Rev. Lett.* **115** 043003
[8] Olmschenk S, Chicireanu R, Nelson K D and Porto J V 2010 Randomized benchmarking of atomic qubits in an optical lattice *New J. Phys.* **12** 113007
[9] Haller E, Hudson J, Kelly A, Cotta D A, Peaudecerf B, Bruce G D and Kuhr S 2015 Single-atom imaging of fermions in a quantum-gas microscope *Nat. Phys.* **11** 738
[10] Lee J H, Montano E, Deutsch I H and Jessen P S 2013 Robust site-resolvable quantum gates in an optical lattice via inhomogeneous control *Nat. Commun.* **4** 2027
[11] Jose S, Surendran P, Wang Y, Herrera I, Krzemien L, Whitlock S, McLean R, Sidorov A and Hannaford P 2014 Periodic array of Bose–Einstein condensates in a magnetic lattice *Phys. Rev.* A **89** 051602
[12] Whitlock S, Gerritsma R, Fernholz T and Spreeuw R J C 2009 Two-dimensional array of microtraps with atomic shift register on a chip *New J. Phys.* **11** 023021
[13] Zobay O and Garraway B M 2001 Two-dimensional atom trapping in field-induced adiabatic potentials *Phys. Rev. Lett.* **86** 1195–8
[14] Reichel J and Vuletic V 2011 *Atom Chips* (New York: Wiley)
[15] van Es J J P, Whitlock S, Fernholz T, van Amerongen A H and van Druten N J 2008 Longitudinal character of atom-chip-based rf-dressed potentials *Phys. Rev.* A **77** 063623
[16] Morizot O, Longchambon L, Easwaran R K, Dubessy R, Knyazchyan E, Pottie P-E, Lorent V and Perrin H 2008 Influence of the radio-frequency source properties on rf-based atom traps *Eur. Phys. J.* D **47** 209–14
[17] Knill E, Leibfried D, Reichle R, Britton J, Blakestad R B, Jost J D, Langer C, Ozeri R, Seidelin S and Wineland D J 2008 Randomized benchmarking of quantum gates *Phys. Rev.* A **77** 012307

[18] Sárkány L, Weiss P, Hattermann H and Fortágh J 2014 Controlling the magnetic-field sensitivity of atomic-clock states by microwave dressing *Phys. Rev.* A **90** 053416
[19] Pethick C J and Smith H 2008 *Bose–Einstein Condensation in Dilute Gases* 2nd edn (Cambridge: Cambridge University Press)
[20] Lesanovsky I, Hofferberth S, Schmiedmayer J and Schmelcher P 2006 Manipulation of ultracold atoms in dressed adiabatic radio-frequency potentials *Phys. Rev.* A **74** 033619
[21] Mischuck B E, Merkel S T and Deutsch I H 2012 Control of inhomogeneous atomic ensembles of hyperfine qudits *Phys. Rev.* A **85** 022302
[22] Sinuco-León G A and Garraway B M 2012 Radio-frequency dressed atoms beyond the linear Zeeman effect *New J. Phys.* **14** 123008
[23] Kazakov G A and Schumm T 2015 Magic radio-frequency dressing for trapped atomic microwave clocks *Phys. Rev.* A **91** 023404
[24] Wildermuth S 2005 One-dimensional Bose–Einstein condensates in micro-traps *PhD Thesis* University of Heidelberg
[25] Craik D P L A, Linke N M, Harty T P, Ballance C J, Lucas D M, Steane A M and Allcock D T C 2014 Microwave control electrodes for scalable, parallel, single-qubit operations in a surface-electrode ion trap *Appl. Phys.* B **114** 3–10
[26] Piltz C, Sriarunothai T, Varón A F and Wunderlich C 2014 A trapped-ion-based quantum byte with 10-5 next-neighbour cross-talk *Nat. Commun.* **5** 4679
[27] Henkel C, Pötting S and Wilkens M 1999 Loss and heating of particles in small and noisy traps *Appl. Phys.* B **69** 379–87
[28] Speelman F 2008 A quantum gate on an atom chip by controlled collisions in state-dependent rf-dressed potentials *Bachelor Monograph* University of Amsterdam
[29] Weitenberg C, Kuhr S, Molmer K and Sherson J F 2011 Quantum computation architecture using optical tweezers *Phys. Rev.* A **84** 032322
[30] Trinker M, Groth S, Haslinger S, Manz S, Betz T, Schneider S, Bar-Joseph I, Schumm T and Schmiedmayer J 2008 Multilayer atom chips for versatile atom micromanipulation *Appl. Phys. Lett.* **92** 254102
[31] Naides M A, Turner R W, Lai R A, DiSciacca J M and Lev B L 2013 Trapping ultracold gases near cryogenic materials with rapid reconfigurability *Appl. Phys. Lett.* **103** 251112
[32] Bernon S *et al* 2013 Manipulation and coherence of ultra-cold atoms on a superconducting atom chip *Nat. Commun.* **4** 2380
[33] Sinuco-León G, Kaczmarek B, Krüger P and Fromhold T M 2011 Atom chips with two-dimensional electron gases: theory of near-surface trapping and ultracold-atom microscopy of quantum electronic systems *Phys. Rev.* A **83** 021401
[34] Surendran P, Jose S, Wang Y, Herrera I, Hu H, Liu X, Whitlock S, McLean R, Sidorov A and Hannaford P 2015 Radio-frequency spectroscopy of a linear array of Bose–Einstein condensates in a magnetic lattice *Phys. Rev.* A **91** 023605
[35] Treutlein P 2008 Coherent manipulation of ultracold atoms on atom chips *PhD Thesis* LMU München
[36] Yan F, Gustavsson S, Bylander J, Jin X, Yoshihara F, Cory D G, Nakamura Y, Orlando T P and Oliver W D 2013 Rotating-frame relaxation as a noise spectrum analyser of a superconducting qubit undergoing driven evolution *Nat. Commun.* **4** 2337
[37] Pegg D T and Series G W 1973 On the reduction of a problem in magnetic resonance *Proc. R. Soc. Lond. Ser.* A **332** 281–9